Pergamon

Int. J. Solids Structures Vol. 32, No. 13, pp. 1927–1947, 1995

0020-7683/95 $9.50 + .00

0020-7683(94)00239-8

INCREMENTAL STRESSES IN LOADED ORTHOTROPIC CIRCULAR MEMBRANE TUBES—II. NUMERICAL SOLUTION

DAN GIVOLI and AVINOAM LIBAI
Department of Aerospace Engineering, Technion—Israel Institute of Technology, Haifa 32000, Israel

(*Received* 11 *April* 1994; *in revised form* 26 *August* 1994)

Abstract—In Part I of this article (1995, *Int. J. Solids Structures* **32**, 1907–1925) a simplified theory for the incremental state of stress in an orthotropic circular membrane tube was presented. In this second part, a numerical method is devised to solve the resulting elliptic sixth-order system of equations, for tubes which contain no slits or holes. In this method, Fourier decomposition is used in the circumferential direction and finite element discretization is used in the longitudinal direction. Special finite elements with six degrees-of-freedom are employed. Using this numerical method, the solutions of several specific problems of membrane tubes are obtained, presented and discussed. These include two problems concerning the decay of boundary disturbances. The theoretical treatment of such decay is also discussed.

1. INTRODUCTION

In the first part of this article (Libai and Givoli, 1994), we presented an incremental linearized theory for the state of stress in an orthotropic circular membrane tube. The tube is initially subjected to uniform internal pressure p_0 (per unit deformed area) and to a pulling force T, which result in a known homogeneous state of stresses accompanied by large homogeneous deformation. The length, thickness and radius of the tube in this homogeneous state are denoted L, h and R [see Fig. 1 of Libai and Givoli (1994)]. At this stage, some changes in the conditions of the tube are considered. These changes may be in the form of additional nonuniform applied loads or of a local change in the geometry, e.g. a small slit (crack) is introduced or the shape of the boundary is slightly changed. We seek the final inhomogeneous deformation and state of stress in the tube. The problem is stated in full detail in Section 4 of Libai and Givoli (1994).

In Libai and Givoli (1994), we derived several versions of the governing equations, with different levels of simplification. One simplified version consists of the elliptic sixth-order linear set of equations (59) and (60) of Libai and Givoli (1994), which are expressed in terms of the stress function ϕ and the curvature function ψ. We repeat these equations here:

$$P_x\psi_{,xx}+P_s\psi_{,ss}+\frac{1}{R}\phi_{,xx}=p(x,s) \tag{1}$$

$$R\nabla_*^4\phi+\psi_{,xx}=0. \tag{2}$$

Here $x\in[0, L]$ and $s\in[0, 2\pi R]$ are distances along the generators and parallel circles of the tube, respectively. Also, a comma indicates partial differentiation, $P_x=T/(2\pi R)$, $P_s=p_0R$ and $p(x,s)$ is the additional (incremental) applied pressure load. The operator ∇_*^4 in eqn (2) is the "modified" biharmonic operator, defined by

$$\nabla_*^4\phi\equiv\beta_x\phi_{,ssss}+\beta_s\phi_{,xxxx}+\rho\phi_{,xxss}. \tag{3}$$

Here β_x, β_s and ρ are constants which depend on the material orthotropic compliances [c_x, c_s, c_{xs}, c_{sx} and c_t in Libai and Givoli (1994)], as well as on the background loads P_x and P_s. These constants are defined in eqns (40)–(44) and (49) of Libai and Givoli (1994). In the case where the material properties are isotropic, ∇_*^4 in eqn (2) reduces to $(1/Eh)\nabla^4$, where E is Young's modulus, and ∇^4 is the proper biharmonic operator.

The assumptions that lead to the simplified equations (1) and (2) can be summarized as follows:

(a) The increments from the homogeneous (reference) state to the final state are sufficiently small to justify the complete linearization of the equations in these increments.
(b) The conditions associated with Donnell's approximation hold. These conditions are expressed in eqns (55) and (56) of Libai and Givoli (1994); they state that the products of the stress resultants *in the homogeneous state* by the strain components are much smaller than the *incremental* stress resultants, and that the same is true for the curvatures. (The effective properties of the highest order terms must, however, be retained.)

In spite of these approximations, the resulting linear equations (1) and (2) include the essential "nonlinear effects" of membrane behavior [see discussion in Section 7 of Libai and Givoli (1994)].

The incremental stress resultants are denoted N_x, N_s and N_t, where the first two are normal stresses and the third is a shear stress. The incremental curvatures are denoted κ_x, κ_s and κ_t, where the first two are normal curvatures and the third is the twist. These stress resultants and curvatures are related to ϕ and ψ via [cf. eqns (57) and (58) of Libai and Givoli (1994)]

$$N_x = \phi_{,ss}, \quad N_s = \phi_{,xx}, \quad N_t = -\phi_{,xs} \tag{4}$$

$$\kappa_x = \psi_{,xx}, \quad \kappa_s = \psi_{,ss}, \quad \kappa_t = \psi_{,xs}. \tag{5}$$

The incremental constitutive relations (35)–(37) of Libai and Givoli (1994) are assumed to hold. In Section 8 of Libai and Givoli (1994), we also argue that if the incremental rotations are small then, under the assumptions (a) and (b) above, ψ is identical to the normal displacement w. In addition, we proposed the boundary conditions of diaphragm (simple) support,

$$\phi = 0; \quad \phi_{,xx} = 0; \quad \psi = 0, \tag{6}$$

as appropriate conditions on the two edges of the tube $x = 0$ and $x = L$ [cf. eqn (65) of Libai and Givoli (1994)]. We recall that the total incremental load acting on the tube is assumed to be self-equilibrated.

In this second part of the article, we shall restrict ourselves to circumferentially "complete" tubes, namely tubes which contain no slits or holes. This restriction is necessary in order that the numerical method proposed here can be applied. The numerical solution of membrane tube problems which involve slits requires additional consideration, for two reasons. First, it necessitates the use of "heavier" numerical tools, such as finite elements with many degrees-of-freedom [see Section 10 of Libai and Givoli (1994)]. Second, one has to specially deal with the singularity at the tip of the slit. As a consequence, the required computational effort is also much larger than when no slits are present. Also, boundary conditions along the generator boundaries have to be included.

The following is the outline of this paper. In Section 2 we apply the Fourier decomposition in the circumferential direction to eqns (1) and (2). This results in an infinite system of uncoupled "modal" ordinary differential equations. In Section 3 we replace each of the modal problems by an equivalent variational problem. In Section 4 we present a finite element formulation for the solution of the variational modal problems. Special finite

elements with six degrees-of-freedom are used in the longitudinal direction of the tube, and their associated matrices are derived explicitly.

The combined finite element–Fourier decomposition method proposed in this paper is less general than some other methods, such as the standard finite element method, in that it can be applied to a more restricted class of problems. In particular, we cannot analyse membranes with slits or holes by using this method. However, for the class of problems considered here (namely problems which involve complete membrane tubes), it is significantly more efficient.

In Section 5 we discuss the calculation of stresses and curvatures, which is performed as a post-process based on the finite element solution. In Section 6 we summarize the numerical procedure and discuss some computational aspects. In Section 7, we use the numerical method to obtain the solutions of several specific problems of membrane tubes. These include two problems concerning the decay of boundary disturbances. The theoretical treatment of such decay is discussed in Appendix A. We close with concluding remarks in Section 8.

2. MODAL EQUATIONS

The first stage in the proposed numerical method is to use the periodicity of the solution in s, and to decompose eqns (1) and (2) *in the circumferential direction* into discrete Fourier modes. To this end, we expand ϕ and ψ in Fourier series of the form:

$$\phi(x,s) = \sum_{n=0}^{\infty}{}' \left[\phi_n^c(x)\cos\frac{ns}{R} + \phi_n^s(x)\sin\frac{ns}{R}\right],$$

$$\psi(x,s) = \sum_{n=0}^{\infty}{}' \left[\psi_n^c(x)\cos\frac{ns}{R} + \psi_n^s(x)\sin\frac{ns}{R}\right]. \tag{7}$$

The prime after the sum indicates a factor of $1/2$ which multiplies the cosine term with $n = 0$. We also decompose $p(x,s)$ in the right side of eqn (1) into its circumferential Fourier modes:

$$p(x,s) = \sum_{n=0}^{\infty}{}' \left[p_n^c(x)\cos\frac{ns}{R} + p_n^s(x)\sin\frac{ns}{R}\right]. \tag{8}$$

Here $p_n^c(x)$ and $p_n^s(x)$ are the known Fourier coefficients of $p(x,s)$, obtained by

$$p_n^c(x) = \frac{1}{\pi R}\int_0^{2\pi R} p(x,s)\cos\frac{ns}{R}\,\mathrm{d}s, \quad p_n^s(x) = \frac{1}{\pi R}\int_0^{2\pi R} p(x,s)\sin\frac{ns}{R}\,\mathrm{d}s. \tag{9}$$

Now we substitute the expansions (7) and (8) into eqns (1) and (2), and require that the coefficients of $\cos(ns/R)$ and those of $\sin(ns/R)$ be balanced on both sides of the equations. After some algebra we obtain

$$R^2 P_s\psi_n'' - n^2 P_s\psi_n + R\phi_n'' = R^2 P_n(x) \tag{10}$$

$$\beta_s R^4\phi_n^{(\mathrm{iv})} - \rho n^2 R^2\phi_n'' + \beta_s n^4\phi_n + R^3\psi_n'' = 0. \tag{11}$$

Here a prime indicates differentiation with respect to x. In eqns (10) and (11) we have omitted the superscripts c and s, since these equations hold equally well for the cosine

coefficients ϕ_n^c and ψ_n^c as for the sine coefficients ϕ_n^s and ψ_n^s. From the boundary conditions (6) we deduce the boundary conditions for the Fourier coefficients at the two edges:

$$\phi_n = 0; \quad \phi_n'' = 0; \quad \psi_n = 0 \quad \text{at} \quad x = 0, L. \tag{12}$$

Thus, we have replaced the original problem (1), (2) and (6) by an infinite sequence of decoupled modal problems, eqns (10)–(12), for $n = 0, 1, 2, \ldots$, which are defined on the one-dimensional interval $[0, L]$.

3. VARIATIONAL MODAL PROBLEM

Now we present a variational formulation for the modal problem (10)–(12). Note that the harmonic number n is considered here to be fixed.

First, we define the two spaces,

$$\mathscr{V}_\phi = \{\phi \mid \phi \in H^2[0, L], \quad \phi = 0 \quad \text{at} \quad x = 0, L\} \tag{13}$$

$$\mathscr{V}_\psi = \{\psi \mid \psi \in H^1[0, L], \quad \psi = 0 \quad at \quad x = 0, L\}. \tag{14}$$

Here H^n is the nth-order Sobolev space. Next, we define the following symmetric and bilinear forms:

$$a(\bar{\phi}, \phi) = \int_0^L (\bar{\phi}'' \beta_s R^4 \phi'' + \bar{\phi}' \rho n^2 R^2 \phi' + \bar{\phi} \beta_x n^4 \phi)\, \mathrm{d}x \tag{15}$$

$$b(\bar{\phi}, \psi) = -\int_0^L \bar{\phi}' R^3 \psi'\, \mathrm{d}x \tag{16}$$

$$c(\bar{\psi}, \psi) = -\int_0^L (\bar{\psi}' R^4 P_x \psi' + \bar{\psi} R^2 n^2 P_s \psi)\, \mathrm{d}x, \tag{17}$$

and the linear form,

$$q(\bar{\psi}) = \int_0^L \bar{\psi} R^4 p_n\, \mathrm{d}x. \tag{18}$$

Then the weak form of the problem (10)–(12) is:

find $\phi_n \in \mathscr{V}_\phi$ and $\psi_n \in \mathscr{V}_\psi$ such that for all $\bar{\phi} \in \mathscr{V}_\phi$ and for all $\bar{\psi} \in \mathscr{V}_\psi$,

$$a(\bar{\phi}, \phi_n) + b(\bar{\phi}, \psi_n) = 0 \tag{19}$$

$$\mathrm{b}(\bar{\psi}, \phi_n) + \mathrm{c}(\bar{\psi}, \psi_n) = \mathrm{q}(\bar{\psi}). \tag{20}$$

It can be proved that this weak form of the problem is equivalent to the strong form consisting of eqns (10)–(12).

It is also possible to recast the problem as a variational principle. To this end, we define the functional $\mathscr{G}$, whose domain is $\mathscr{V}_\phi \times \mathscr{V}_\psi$:

$$\mathscr{G}[\phi, \psi] = \tfrac{1}{2} a(\phi, \phi) + \tfrac{1}{2} c(\psi, \psi) + b(\phi, \psi) - q(\psi). \tag{21}$$

Then we seek the pair (ϕ_n, ψ_n) which makes $\mathscr{G}$ stationary. It is easy to see that by requiring that the first variations of $\mathscr{G}$ with respect to ϕ and to ψ vanish, one obtains the two equations

(19) and (20). Thus, the stationary point (ϕ_n, ψ_n) of $\mathscr{G}$ is also the solution to eqns (10)–(12). This stationary point is unique and is a saddle point (Sewell, 1987).

This variational formulation is analogous to the one presented in Section 9.1 of Libai and Givoli (1994) for the full two-dimensional problem. For other types of boundary conditions and reference states, the more general functional Π^*, introduced in Section 9.2 of Libai and Givoli (1994), can be exploited.

4. FINITE ELEMENT FORMULATION

Now we use the weak form of the modal problem, (19) and (20), as the starting point for a Galerkin finite element scheme. This scheme has the standard form of a mixed-type finite element formulation which is often used in other contexts (Malkus and Hughes, 1978; Kikuchi, 1987; Stenberg, 1988; Roberts and Thomas, 1991). Note that the finite element method is applied to each modal problem separately, and thus is associated with the *longitudinal* discretization of the tube. On the other hand, in the *circumferential* direction the discretization is spectral, as described in Section 2.

The combination of finite elements in one spatial direction and discrete Fourier decomposition in another spatial direction is a known technique, and has been employed previously in various studies [see e.g. Rand and Givoli (1992), Givoli and Rand (1993), Bathe and Almeida (1980), Wunderlich *et al.* (1985), Danielson and Tielking (1993), Kaiser *et al.* (1993), and Akhras *et al.* (1993)]. The "finite strip" approach is one example of such a technique. Here we shall apply a combined finite element–Fourier decomposition method to the membrane problem under consideration. This will lead to a nonstandard but very efficient numerical scheme.

In the Galerkin finite element method, we replace the spaces $\mathscr{V}_\phi$ and $\mathscr{V}_\psi$ by finite-dimensional subspaces $\mathscr{V}_\phi^h$ and $\mathscr{V}_\psi^h$. The functions $\phi^h \in \mathscr{V}_\phi^h$ and $\psi^h \in \mathscr{V}_\psi^h$ are assumed to have the form:

$$\phi^h(x) = \sum_A N_A^{(1)}(x)\phi_A + \sum_A N_A^{(2)}(x)\chi_A \tag{22}$$

$$\psi^h(x) = \sum_A M_A(x)\psi_A. \tag{23}$$

Here the index A corresponds to a node number in the finite element mesh, $N_A^{(1)}$, $N_A^{(2)}$ and M_A are shape functions associated with node A, and ϕ_A, χ_A and ψ_A are the nodal values of ϕ^h, $\phi^{h\prime}$ and ψ^h, respectively. Note that the special structure of eqn (22) is needed due to the regularity condition $\phi \in H^2$ in eqn (13), which leads to the requirement that both ϕ^h *and* $\phi^{h\prime}$ be continuous in $[0, L]$. Thus, the shape functions $N_A^{(1)}$ and $N_A^{(2)}$ in eqn (22) must be continuously differentiable in $[0, L]$. On the other hand, the lower-order regularity condition $\psi \in H^1$ in eqn (14) allows the use of shape functions M_A in eqn (23) which are continuous but only piecewise-differentiable. For a discussion on the regularity requirements of finite element shape functions, see e.g. Hughes (1987).

The finite element solution-pair of the modal problem (19) and (20), ϕ_n^h and ψ_n^h, as well as the weighting functions $\bar{\phi}$ and $\bar{\psi}$, are expanded as in eqns (22) and (23). Then the resulting expressions are substituted into eqns (19) and (20), and the linearity of the forms (15)–(18) as well as the arbitrariness of the coefficients in the expansions of $\bar{\phi}$ and $\bar{\psi}$ is exploited. This results in the global finite element system of equations:

$$\mathbf{K}_n \mathbf{d}_n = \mathbf{F}_n, \tag{24}$$

where $\mathbf{K}_n$ is the "stiffness matrix," $\mathbf{F}_n$ is the "load vector" and $\mathbf{d}_n$ is the solution vector, whose entries are the unknown nodal values ϕ_A, χ_A and ψ_A, alternately.

As usual in finite element formulations, it is convenient to describe all the quantities and do all the calculations on the element level. Thus, we shall obtain explicit expressions for the element stiffness matrix $\mathbf{k}^e$ and the element load vector $\mathbf{f}^e$. Here we omit the index n

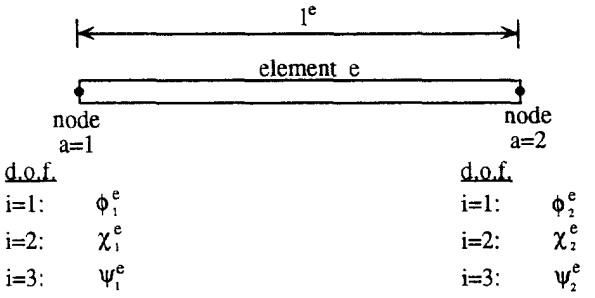

Fig. 1. The finite element used in the solution of the modal problem. Three degrees-of-freedom are associated with each node, i.e. the nodal values of ϕ, ϕ' and ψ (denoted ϕ_a, χ_a and ψ_a).

corresponding to the mode number, for clarity. The global matrix $\mathbf{K}_n$ and global vector $\mathbf{F}_n$ are obtained from the element matrices $\mathbf{k}^e$ and the element load vectors $\mathbf{f}^e$, respectively, by applying the standard assembly operator. For future reference, we define the forms $a(\cdot,\cdot)^e$, $b(\cdot,\cdot)^e$, $c(\cdot,\cdot)^e$ and $q(\cdot)^e$ exactly as in eqns (15)–(18), but with the integration performed only over the domain of element e.

A single element is shown in Fig. 1. It has two nodes, and three degrees of freedom at each node: the nodal values of ϕ_n^h, $\phi_n^{h\prime}$ and ψ_n^h. Inside each element, the functions ϕ_n^h and ψ_n^h are interpolated, analogously to eqns (22) and (23), via

$$\phi_n^h(x) = \sum_{a=1}^{2} N_a^{(1)}(x)\phi_{na} + \sum_{a=1}^{2} N_a^{(2)}(x)\chi_{na}, \quad x \in \Omega^e \tag{25}$$

$$\psi_n^h(x) = \sum_{a=1}^{2} M_a(x)\psi_{na}, \quad x \in \Omega^e. \tag{26}$$

Here Ω^e is the element domain, and the index a corresponds to an element node number ($a = 1, 2$). The shape functions $N_a^{(1)}, N_a^{(2)}$ and M_a are the element counterparts of the "global" shape functions $N_A^{(1)}, N_A^{(2)}$ and M_A. We choose M_a to be the standard *linear* shape functions, and $N_a^{(1)}$ and $N_a^{(2)}$ to be the *Hermite cubic* shape functions, which are often used in Bernoulli–Euler beam bending problems (Hughes, 1987).

The element stiffness matrix $\mathbf{k}^e$ is a 6×6 matrix, whose entries may be written as k^e_{IJ}. However, it is more convenient to write the entries of $\mathbf{k}^e$ as k^e_{aibj}, using four indices. Here a and b correspond to node numbers and range from 1 to 2, and i and j correspond to degree-of-freedom numbers and range from 1 to 3 (see Fig. 1). The relations $I = 3(a-1)+i$ and $J = 3(b-1)+j$ hold, and thus, for example, $k^e_{23} \equiv k^e_{1213}$. Using this description, it is easy to obtain

$$k^e_{aibj} = \begin{cases} a(N_a^{(i)}, N_b^{(j)})^e; & i = 1,2, \quad j = 1,2 \\ b(N_a^{(i)}, M_b)^e; & i = 1,2, \quad j = 3 \\ b(M_a, N_b^{(j)})^e; & i = 3, \quad j = 1,2 \\ c(M_a, M_b)^e; & i = 3, \quad j = 3 \end{cases}. \tag{27}$$

To obtain $\mathbf{k}^e$ in explicit form, we now substitute the well known expressions for the linear shape functions M_a and the Hermite cubics $N_a^{(i)}$ (Hughes, 1987) into eqn (27), use the definitions (15)–(17), and perform the resulting integrations exactly. After some algebra, we finally get

$$\mathbf{k}^e = \frac{\beta_s R^4}{(l^e)^3}\begin{bmatrix} 12 & 6h & 0 & -12 & 6h & 0 \\ & 4h^2 & 0 & -6h & 2h^2 & 0 \\ & & 0 & 0 & 0 & 0 \\ & & & 12 & -6h & 0 \\ & & & & 4h^2 & 0 \\ & & & & & 0 \end{bmatrix} + \frac{\rho n^2 R^2}{30 l^e}\begin{bmatrix} 36 & 3h & 0 & -36 & 3h & 0 \\ & 4h^2 & 0 & -3h & -h^2 & 0 \\ & & 0 & 0 & 0 & 0 \\ & & & 36 & -3h & 0 \\ & & & & 4h^2 & 0 \\ & & & & & 0 \end{bmatrix}$$

$$+ \frac{\beta_x n^4 l^e}{420}\begin{bmatrix} 156 & 22h & 0 & 54 & -13h & 0 \\ & 4h^2 & 0 & 13h & -3h^2 & 0 \\ & & 0 & 0 & 0 & 0 \\ & & & 156 & -22h & 0 \\ & & & & 4h^2 & 0 \\ & & & & & 0 \end{bmatrix} - \frac{R^4 P_x}{l^e}\begin{bmatrix} 0 & 0 & 0 & 0 & 0 & 0 \\ & 0 & 0 & 0 & 0 & 0 \\ & & 1 & 0 & 0 & -1 \\ & & & 0 & 0 & 0 \\ & & & & 0 & 0 \\ & & & & & 1 \end{bmatrix}$$

$$- \frac{R^2 n^2 P_s l^e}{6}\begin{bmatrix} 0 & 0 & 0 & 0 & 0 & 0 \\ & 0 & 0 & 0 & 0 & 0 \\ & & 2 & 0 & 0 & 1 \\ & & & 0 & 0 & 0 \\ & & & & 0 & 0 \\ & & & & & 2 \end{bmatrix} + \frac{R^3}{l^e}\begin{bmatrix} 0 & 0 & -1 & 0 & 0 & 1 \\ & 0 & 0 & 0 & 0 & 0 \\ & & 0 & 1 & 0 & 0 \\ & & & 0 & 0 & -1 \\ & & & & 0 & 0 \\ & & & & & 0 \end{bmatrix}. \tag{28}$$

Here l^e is the length of the element (see Fig. 1). All the matrices that appear in eqn (28) are symmetric, and so only their upper half is indicated. We note that most of these matrices are proportional to the well-known finite element matrices used in linear one-dimensional rod and beam analysis (Hughes, 1987; Cook *et al.*, 1989). More specifically, the nonzero blocks of the first five matrices on the right hand side of eqn (28) are proportional, by order, to the stiffness matrix of a Bernoulli–Euler beam element, the geometric stiffness matrix of a beam element (used, for example, in buckling analysis), the mass matrix of a beam element, the stiffness matrix of a tension-compression rod element and the mass matrix of a rod element.

Now we turn to the element load vector $\mathbf{f}^e$. As before, we use the two indices ai $(a = 1,2; i = 1,2,3)$ for the entries of $\mathbf{f}^e$ instead of the single index $I (I = 1,\ldots,6)$, where $I = 3(a-1)+i$. It is easy to show that

$$f^e_{ai} = q\,(M_a)^e \delta_{i3}, \tag{29}$$

where δ_{ij} is the Kronecker delta. To obtain an explicit expression for $\mathbf{f}^e$, we first interpolate the pressure $p_n(x)$ linearly inside the element between its two nodal values p^e_{n1} and p^e_{n2}. Then we substitute the expression for M_a in eqn (29) and use the definition (18) to finally get

$$\mathbf{f}^e = \frac{R^4 l^e}{6}\begin{Bmatrix} 0 \\ 0 \\ 2p^e_{n1} + p^e_{n2} \\ 0 \\ 0 \\ p^e_{n1} + 2p^e_{n2} \end{Bmatrix}. \tag{30}$$

We also consider the case where the pressure $p_n(x)$ is proportional to the Dirac delta with singularity at node B, i.e. $p_n(x) = P\delta(x - x_B)$, where x_B is the location of node B. This representation allows us to consider forces which are concentrated in the x direction (see

examples in Section 7). It is most convenient to account for these concentrated forces by adding their contribution directly to the global load vector **F** [the right hand side of eqn (24)]. Analogously to eqn (29), it is clear that $F_{Ai} = q(M_A)\delta_{i3}$, where A indicates a global node number and M_A denotes the global shape function associated with node A. Using eqn (18) we obtain

$$F_{Ai} = R^4 P \delta_{AB} \delta_{i3}. \tag{31}$$

Thus, the quantity R^4P must be added to the entry in the global force vector which corresponds to degree-of-freedom 3 of node B (where the "concentrated load" acts).

5. CALCULATION OF STRESSES AND CURVATURES

The finite element system of equations (24) is considered for a desired finite number of modes $n = 0, \ldots, N$. For each mode $n \geqslant 1$, two problems have to be solved: one for the cosine Fourier coefficients and one for the sine coefficients. The mode $n = 0$ gives one additional problem. Thus, we solve altogether $2N+1$ problems of the form (24). In each case we obtain the solution vector $\mathbf{d}_n$, namely the nodal values ϕ_{nA}, χ_{nA} and ψ_{nA}, for all nodes A.

Now it is possible to calculate the stress resultants and curvatures at desired points of the tube. We substitute eqn (7) into eqns (4) and (5) to obtain expressions for the stresses and curvatures. For example, we obtain

$$N_x(x,s) = -\sum_{n=0}^{N}{}' \left(\frac{n}{R}\right)^2 \left[\phi_n^c(x)\cos\frac{ns}{R} + \phi_n^s(x)\sin\frac{ns}{R}\right], \tag{32}$$

and similar expressions for the other stress and curvature components. In eqn (32) we omitted the superscript h for clarity, although all the quantities which appear throughout this section are based on the finite element approximation. Now we can easily extract the following expressions for the corresponding Fourier coefficients:

$$(N_x)_n^c = -(n/R)^2\phi_n^c(x), \quad (N_x)_n^s = -(n/R)^2\phi_n^s(x) \tag{33}$$

$$(N_s)_n^c = \phi_n^{c\prime\prime}(x), \quad (N_s)_n^s = \phi_n^{s\prime\prime}(x) \tag{34}$$

$$(N_t)_n^c = -(n/R)\phi_n^{s\prime}(x), \quad (N_t)_n^s = (n/R)\phi_n^{c\prime}(x) \tag{35}$$

$$(\kappa_x)_n^c = \psi_n^{c\prime\prime}(x), \quad (\kappa_x)_n^s = \psi_n^{s\prime\prime}(x) \tag{36}$$

$$(\kappa_s)_n^c = -(n/R)^2\psi_n^c(x), \quad (\kappa_s)_n^s = -(n/R)^2\psi_n^s(x) \tag{37}$$

$$(\kappa_t)_n^c = (n/R)\psi_n^{s\prime}(x), \quad (\kappa_t)_n^s = -(n/R)\psi_n^{c\prime}(x). \tag{38}$$

As before, it is convenient to perform all the calculations on the element level. In particular, we choose to calculate the stresses and curvatures *at the mid-point* of each element. To this end, we denote the position x of the mid-point of element e by x_0^e. We substitute eqns (25) and (26) into eqns (33)–(38) [except eqn (36); see later], use the known explicit expressions for the linear and Hermite cubic shape functions (Hughes, 1987) and set $x = x_0^e$. After some algebra we obtain

$$(N_x^c)_n \equiv (N_x)_{n|_{x=x_m^e}} = -\left(\frac{n}{R}\right)^2 \left[\frac{1}{2}(\phi_{n1}^e + \phi_{n2}^e) - \frac{1}{8} l^e (\chi_{n2}^e - \chi_{n1}^e)\right] \tag{39}$$

$$(N_s^e)_n \equiv (N_s)_{n|_{x=x_m^e}} = \frac{1}{l^e}(\chi_{n2}^e - \chi_{n1}^e) \tag{40}$$

$$(N_t^e)_n \equiv (N_t)_{n|_{x=x_m^e}} = -\alpha \frac{n}{R}\left[\frac{3}{2l^e}(\phi_{n2}^e - \phi_{n1}^e) - \frac{1}{4}(\chi_{n1}^e + \chi_{n2}^e)\right]^* \tag{41}$$

$$(\kappa_x^e)_n \equiv (\kappa_x)_{n|_{x=x_m^e}} = -\frac{1}{2}\left(\frac{n}{R}\right)^2 (\psi_{n1}^e + \psi_{n2}^e) \tag{42}$$

$$(\kappa_t^e)_n \equiv (\kappa_t)_{n|_{x=x_m^e}} = \alpha \frac{n}{R}\frac{1}{2}[\psi_{n2}^e - \psi_{n1}^e]^*. \tag{43}$$

Here ϕ_{n1}^e, ϕ_{n2}^e, χ_{n1}^e, χ_{n2}^e, ψ_{n1}^e and ψ_{n2}^e are the nodal values at the two nodes of element e. In eqns (39), (40) and (42) we have omitted the cosine and sine superscripts (c and s) since the equations are identical for both. In eqns (41) and (43), α is defined to be 1 if the quantity on the left side is a cosine Fourier coefficient and -1 if it is a sine coefficient. Also, the asterisk after the brackets in eqns (41) and (43) indicates that the values which appear in the brackets are those corresponding to the *cosine* solution if the quantity on the left side is a *sine* Fourier coefficient, and vice versa.

We have not yet given the expression for the Fourier coefficients of the axial curvature κ_x. The reason is that in eqn (36) the second derivative of the function ψ_n appears. Now, since $\psi_n(x)$ is expanded via the shape functions M_A [see eqn (23)], which are not continuously differentiable, we cannot obtain the second derivative of ψ_n by directly differentiating eqn (23) or (26) twice. However, we may calculate κ_x from κ_s and N_s by using eqn (25) of Libai and Givoli (1994), which is the linearized normal equilibrium equation,

$$P_x \kappa_x + P_s \kappa_s + \frac{1}{R} N_s = p. \tag{44}$$

From eqn (44) we deduce

$$(\kappa_x^c)_n \equiv (\kappa_x)_{n|_{x=x_m^e}} = \frac{1}{P_x}\left[p_n^e - P_s(\kappa_s^e)_n - \frac{(N_s^e)_n}{R}\right]. \tag{45}$$

Here p_n^e is the value of p_n at the mid-point of element e.

Thus, the Fourier components of the stress resultants and curvatures may easily be obtained via eqns (39)–(43) and (45), based on the finite element solution of the cosine and sine problems for each mode n. We note that while the finite element solution of the cosine (sine) problem for mode n yields the cosine (sine) coefficients of N_x, N_s, κ_x and κ_s, it yields the sine (cosine) coefficients of the shear stress N_t and the twist κ_t. Of course, this should be taken into account when superposing the different modal solutions, as described in the next section.

6. THE NUMERICAL PROCEDURE AND COMPUTATIONAL ASPECTS

The numerical scheme described in the previous sections may be summarized by the following algorithm:

1. Read input parameters.
2. Loop on harmonics: $n = 0, \ldots, N$.

3. For all elements e: form the element stiffness matrix $\mathbf{k}_n^e$ using eqn (28), and assemble it into the global stiffness matrix $\mathbf{K}_n$.
4. Factorize $\mathbf{K}_n$.
5. Loop: $i = \cos$ or $\sin$.
6. Read Fourier coefficients of nodal concentrated loads, and insert them in the global load vector $\mathbf{F}_n$ using eqn (31).
7. Read Fourier coefficients of distributed element loads, form the element load vectors $\mathbf{f}_n^e$ of all loaded elements using eqn (30), and assemble into $\mathbf{F}_n$.
8. Solve $\mathbf{K}_n\mathbf{d}_n = \mathbf{F}_n$.
9. Superpose the current modal solution $\mathbf{d}_n$ to the total solution vector $\mathbf{d}$.
10. Calculate the current mid-point modal stresses and curvatures using eqns (39)–(43) and (45).
11. Superpose the current modal stresses and curvatures to the total stress and curvature solution arrays
12. Next i.
13. Next n.
14. Print the solution vector $\mathbf{d}$ and all the mid-point stresses and curvatures at desired s locations.

We now make a few remarks regarding this scheme.

In step 3, if all the elements are of the same length then it is sufficient to form the element stiffness matrix $\mathbf{k}_n^e$ once, since all the element matrices are identical in this case. In steps 6 and 7 we have to read the Fourier coefficients of the given concentrated and distributed loads. These coefficients are most conveniently calculated as a pre-process by applying a Fast Fourier Transform (FFT) software to the given load function p. In step 8, only forward reduction and back substitution have to be performed to obtain $\mathbf{d}_n$, since the matrix $\mathbf{K}_n$ has been factorized in step 4.

In step 9, the superposition of the modal solution to the total solution is performed by employing the updating formula

$$\mathbf{d} \leftarrow \mathbf{d} + \mathbf{d}_n T^i(ns/R), \tag{46}$$

where $T^i(t)$ is either $\cos t$ or $\sin t$, according to the "value" of i in step 5. Similarly, in step 11, the normal stresses and curvatures are superposed using an updating formula of the form (46). The shear stress $(N_t^e)_n$ and the twist $(\kappa_t^e)_n$ are also superposed using such a formula, but with a "reversed" $T^i(t)$, i.e. $T^i(t) = \cos t$ if $i = \sin$ and $T^i(t) = \sin t$ if $i = \cos$. This procedure follows from eqns (41) and (43), where we recall that the asterisk indicates the "reversal" of the trigonometric function.

In step 14, the final results are reported. These include all the nodal values of ϕ, ϕ' and ψ, and all the elemental mid-point stress resultants and curvatures, at desired circumferential locations. We recall that under the assumptions stated in Section 1, ψ has the physical meaning of the normal displacement.

To close this section, we discuss the appropriate choice for N, the number of harmonics in the Fourier decomposition used in the s direction. N must be large enough so that two Fourier representations are satisfactory: that of the given load and that of the unknown solution. The solution is expected to be quite smooth even if the given load is discontinuous or singular (Dirac delta). Thus, it is reasonable to assume that the number of harmonics N used in the solution process is sufficient if the given load may be represented adequately by a linear combination of the first N modes. This easily leads to a conservative estimate for the appropriate value of N. A more efficient procedure is to check, during the solution process, the contribution of each modal solution to the total solution, and to stop the process if this contribution is smaller than a certain given tolerance ε. Thus, from eqn (46) we may derive the "convergence criterion",

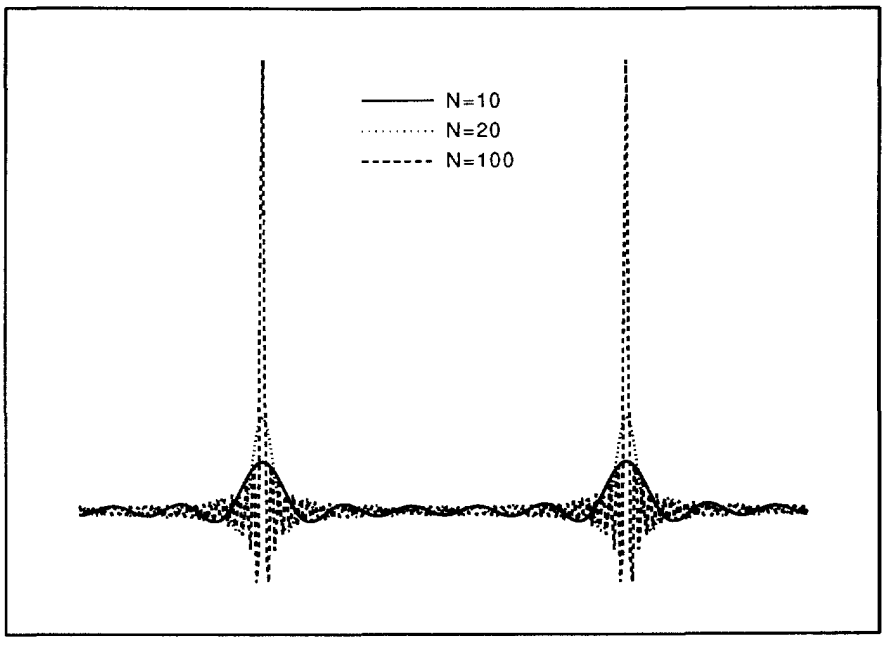

Fig. 2. Fourier series representation of two opposite concentrated forces with different numbers of terms.

$$\|\mathbf{d}_n\|/\|\mathbf{d}\| < \varepsilon, \tag{47}$$

where $\|\mathbf{d}\|$ is the Eulerian norm of the vector $\mathbf{d}$. Note that $\mathbf{d}$ in inequality (47) should be the updated $\mathbf{d}$ on the left hand side of eqn (46), to avoid division by zero in the very first step.

When the given load is a smoothly distributed load, usually the first few modes would be sufficient to represent it. On the other hand, Fourier series representation is not so efficient for very nonsmooth data or for data with a local nature. If the load has the character of a step-function or of a Dirac delta (concentrated load), then many harmonics may be needed for appropriate representation. Note, however, that the smoothness discussed here pertains only to the behavior of the load *in the* s *direction* and not in the x direction. In the axial direction, local features are resolved by the finite element discretization, provided that the finite element mesh is fine enough in regions where the solution changes rapidly. See Fletcher (1984) for a comparison of spectral and finite element Galerkin methods in this and other respects.

As an example, consider the case of two equal and opposite concentrated point loads Q acting at the center of the tube (see example 4 in the next section). In this case the load is $p(x,\theta) = Q\delta(x-L/2)[\delta(\theta)+\delta(\theta-\pi)]$, where $\delta(\theta)$ is the Dirac delta and $\theta = s/R$ ranges from 0 to 2π. From eqns (8) and (9), the truncated Fourier representation in the s direction is

$$p(x,\theta) \simeq Q\delta(x-L/2)\left[\frac{1}{\pi}+\frac{2}{\pi}\sum_{n=2,4,6,\ldots}^{N}\cos n\theta\right]. \tag{48}$$

Figure 2 shows the function in brackets for $N = 10$, $N = 20$ and $N = 100$. *In example* 4 *of the next section, we used* $N = 100$, since further increase in N changed the numerical results only slightly according to criterion (47).

7. EXAMPLE PROBLEMS AND NUMERICAL SOLUTIONS

In this section we test the proposed solution procedure and present some numerical results. Examples 1 and 2 are test problems whose exact solutions (under the theory considered) are easily obtained. We compare these exact solutions to the solutions generated

by the numerical scheme. Examples 3–7 further demonstrate the performance of the scheme. In all the examples, the membrane material is chosen to be *isotropic*, with Young's modulus E [see eqn (62) of Libai and Givoli (1994)].

Example 1 : *axisymmetric-parabolic load*

Consider the following load, which is uniform in s and parabolic in x:

$$p(x,s) = \frac{Eh}{LR^2} x(L-x) + \frac{2}{L} P_x. \tag{49}$$

It is easy to verify that the exact solution to eqns (1), (2) and (6) with this given load is

$$\phi = \frac{Eh}{12LR} x(-x^3 + 2Lx^2 - L^3) \tag{50}$$

$$\psi = -\frac{x}{L}(L-x). \tag{51}$$

Now we set $L = 1$, $R = 0.1$, $Eh = 1$, $P_x = 10$, $P_s = 1$, and we use 10 identical finite elements. Due to the axisymmetry of the problem, the numerical solution remains the same regardless of N; only the $n = 0$ modal solution makes a nonzero contribution to the total solution vector **d**. Note also that in the axisymmetric case the numerical solution (as well as the exact solution) does not depend on the initial pressure P_s. This follows from eqn (28), where P_s appears only in the coefficient of the fifth matrix, multiplied by n^2. [That the exact solution does not depend on P_s in the axisymmetric case can be deduced directly from eqns (1) and (2).]

We compare the exact solution for ψ, N_s and κ_x to the numerical results. The relative errors in these three variables at the center of the tube ($x = L/2$) are 0.005%, 1% and 1%, respectively. The maximal relative errors in these variables are 0.005%, 5% and 5%, respectively. Thus, the error in ψ is extremely small, and the error in N_s and κ_x is reasonably small for the given crude mesh. This difference between the accuracy of the primary variables (ϕ, χ and ψ) and the accuracy of the "second-derivative" variables (stresses and curvatures) is of course expected. Refining the finite element mesh leads to further reduction in these errors. This example demonstrates that the accuracy of the numerical scheme is satisfactory for "smooth" axisymmetric loading.

Example 2 : *axisymmetric ring load*

We consider an axisymmetric ring shear force, acting at the center of the tube, $x = L/2$. Thus, $p = Q\delta(x - L/2)$. We set $Q = 1$, $L = 100$, $R = 1$, $Eh = 1$, $P_s = 1$, and we use 100 identical finite elements. We solve the problem numerically with four different values of the longitudinal initial force : $P_x = 100$, 10, 1 and 0.1. Figure 3 shows the hoop stress N_s along the tube for these values of P_x. As expected, the distribution of the hoop stress becomes more local and its peak becomes higher as the initial axial tension in the tube is decreased. For $P_x = 10$, we have compared the numerical solution to the exact solution of this problem, and again obtained a very good agreement between the two. In Fig. 3 and in all the other graphs that follow, the results for the stresses and curvatures are linearly interpolated between the element mid-points.

For $P_x = 0.1$, the solution shown in Fig. 3 exhibits an "overshoot" on both sides of the loaded point. This is a numerical artifact, which can be explained by noting that for small values of P_x the problem (1), (2) and (6) becomes a singular perturbation problem. Overshoot, spurious oscillations and "locking" are well known numerical effects associated with the finite element solution of such problems [see e.g. Hughes (1987), Babuska and Szymczak (1982), Stolarsky and Belytschko (1983) and Givoli (1988)]. Various ways to overcome these undesired effects have been proposed [see e.g. Hughes (1987)]. However, it must be noted that the tube theory under consideration ceases to be applicable when P_x

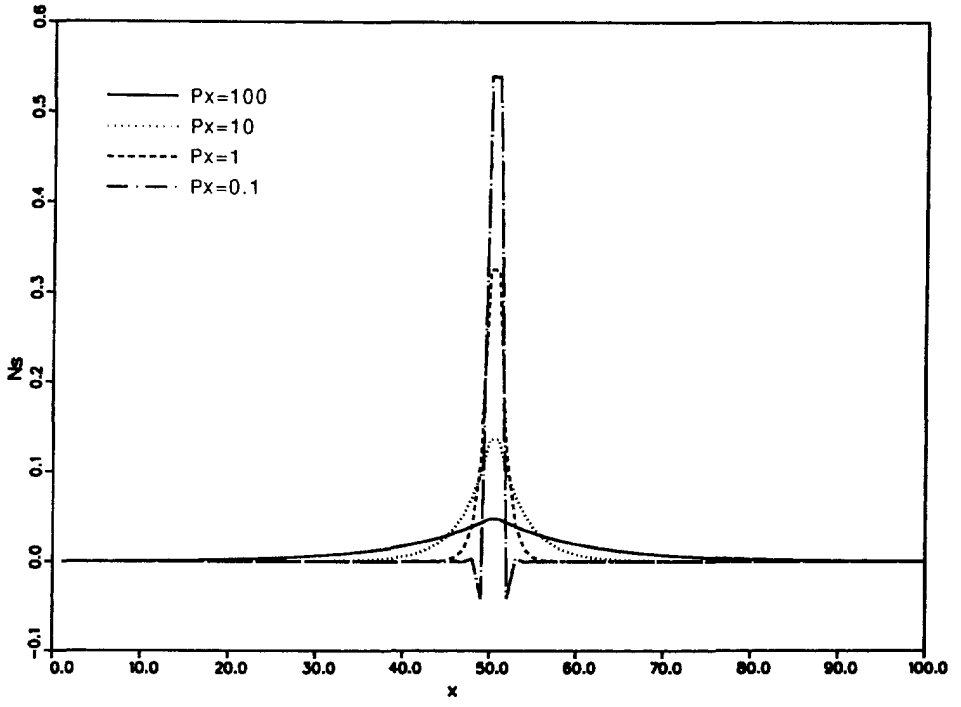

Fig. 3. The axisymmetric ring load problem: the hoop stress N_s along the tube for different values of P_x.

becomes small compared with Q, since in this case the problem becomes strongly nonlinear, and linearization about the reference homogeneous state may not be justified. Thus, the *exact* solution of eqns (1), (2) and (6), not only the numerical solution, becomes physically meaningless when P_x becomes small.

Example 3: *a cos 2θ load along an axial segment*

We consider a tube of length $L = 100$, whose central segment $40 \leqslant x \leqslant 60$ is loaded by the pressure $p = \cos 2\theta$ (where $\theta = s/R$). The parameters are the same as in the previous example. Here, only the cosine part of the mode $n = 2$ contributes to the solution. Figure 4 shows the normal displacement ψ along the axial line $\theta = 0$ for four values of P_x. As P_x becomes smaller, the displacement pattern is localized and approaches the shape of a "rectangular step", which is also the pattern of the load in the x direction. Again, the numerical solution corresponding to $P_x = 0.1$ exhibits spurious overshoot.

Example 4: *pinched tube*

We consider two equal and opposite concentrated point loads $Q = 1$ pinching the tube at its central cross-section $x = L/2$, at the circumferential positions $\theta = 0$ and $\theta = \pi$. This case is discussed at the end of Section 6, and the Fourier decomposition of p in this case is given by eqn (48). The parameters are the same as in example 2. We use $N = 100$ harmonics in the s direction. We obtain the numerical results for different values of P_x, as before.

Figures 5–8 summarize the results. Figure 5 shows the normal displacement ψ along the perimeter of the central cross-section $x = L/2$. Figure 6 shows the normal stress components N_x and N_s, and Fig. 7 shows the shear stress $|N_t|$ along this perimeter. In Fig. 8, the normal curvature κ_s is shown along the axial line $\theta = 0$. The curvature κ_s behaves similarly. The twist $|\kappa_t|$ is extremely small throughout the tube, for all values of P_x considered.

Example 5: *beam-like loading*

We consider a membrane tube of length $L = 100$ loaded with the "beam-like load" illustrated in Fig. 9. The load function $p(x, \theta)$ may be written as $p = \delta(\theta - \pi)S(x) +$

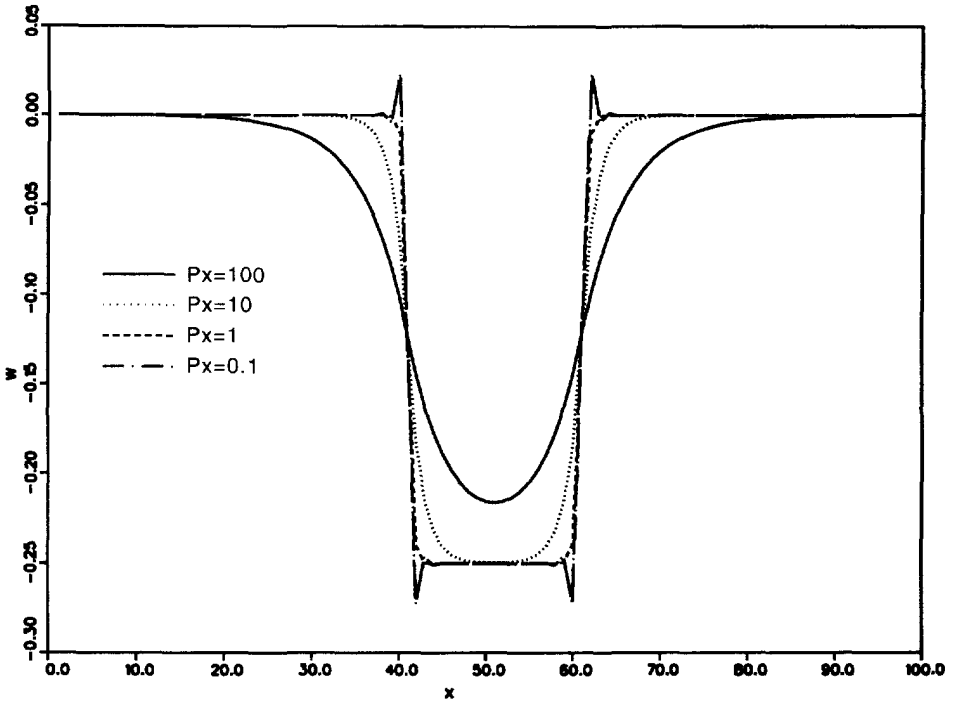

Fig. 4. The $\cos 2\theta$ load problem: the normal displacement ψ along the axial line $\theta = 0$ for different values of P_x.

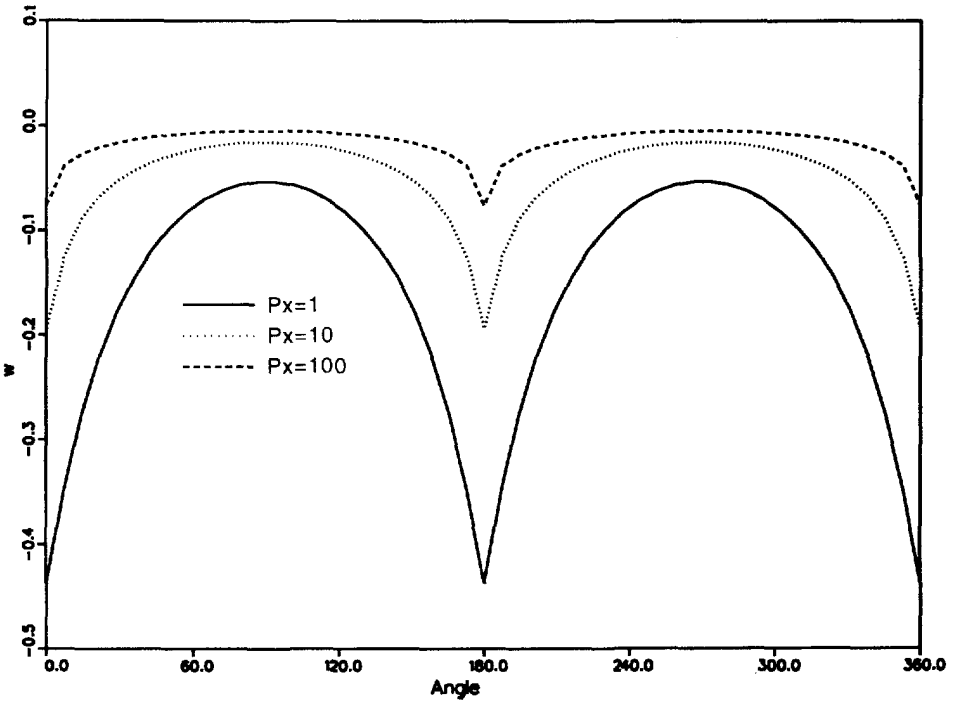

Fig. 5. The pinched tube problem: the normal displacement ψ along the central perimeter of the tube.

$10\delta(x-30)\delta(\theta)+10\delta(x-70)\delta(\theta)$, where $S(x)$ is defined as having the value 1 if $40 \leqslant x \leqslant 60$ and 0 otherwise. The parameters are the same as in example 2, and we use $N = 100$ harmonics. In this example we also set $P_x = 10$.

Figures 10 and 11 show the stress components N_x and N_s, respectively, along the axial lines $\theta = \bar{\theta}$, for the angular values $\bar{\theta} = 0$, 90 and 180°. Whereas the distribution of N_x along

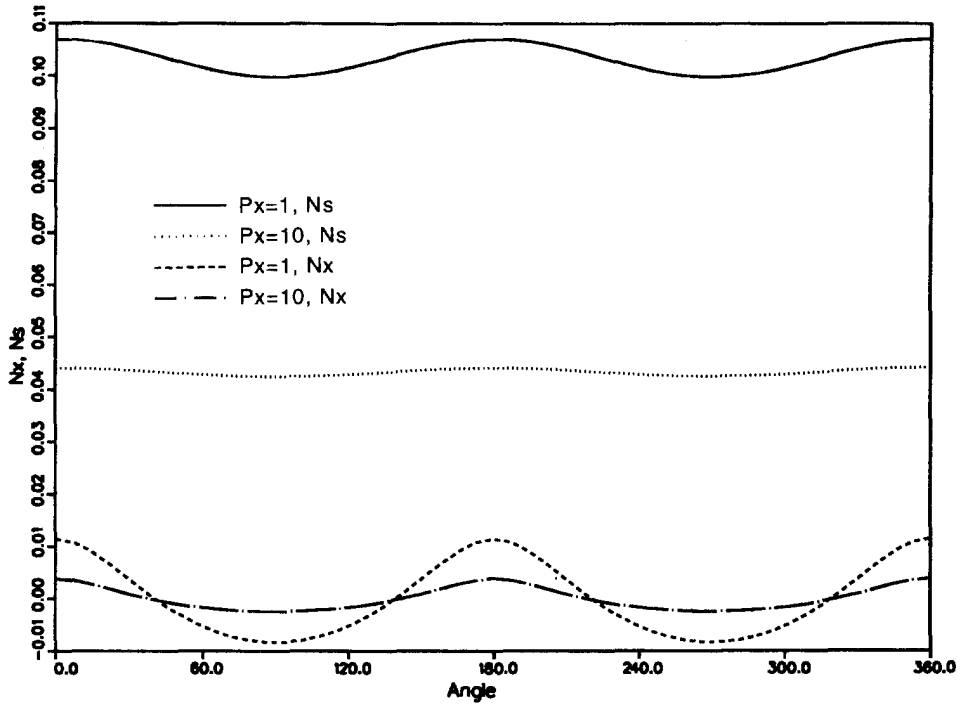

Fig. 6. The pinched tube problem: the normal stress components N_x and N_s along the central perimeter of the tube.

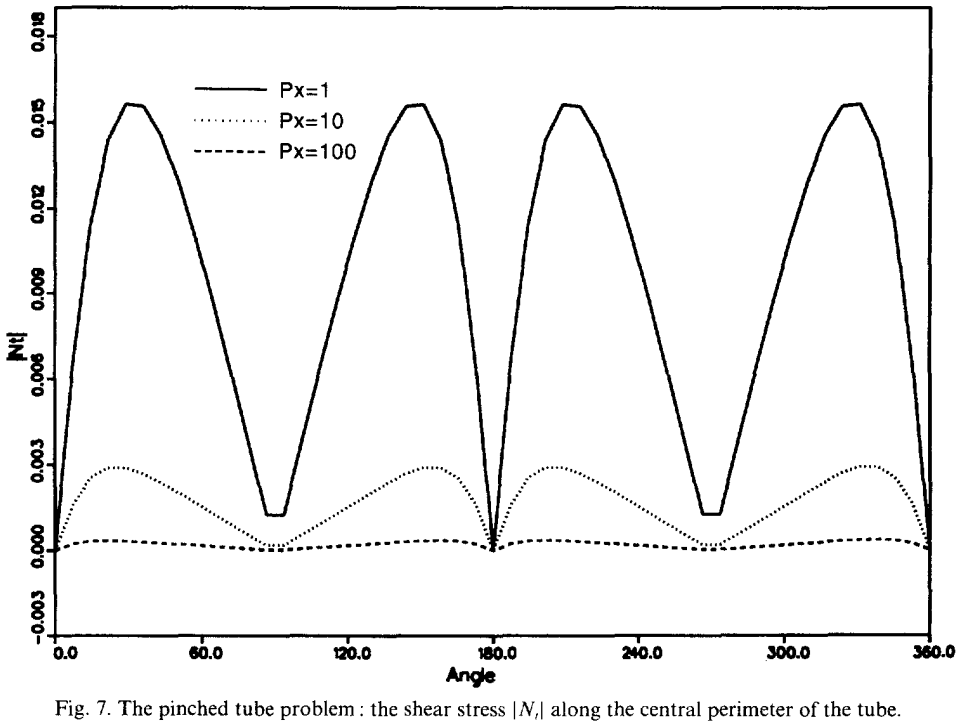

Fig. 7. The pinched tube problem: the shear stress $|N_t|$ along the central perimeter of the tube.

the tube differs significantly from one axial line to another, the hoop stress N_s is seen to depend very weakly on θ; the various graphs differ only near the two points of application of the concentrated forces.

Example 6: *ovalization of the boundary*

In all the previous examples, the perturbation of the homogeneous reference state was in the form of normal loading. In this and the following example we perturb the deformation

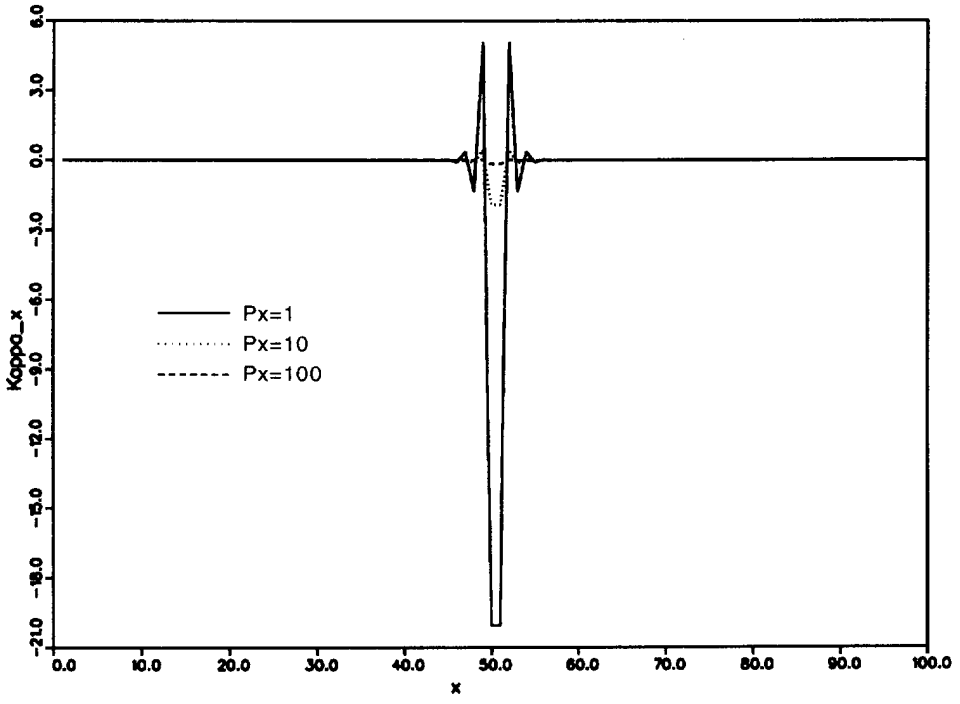

Fig. 8. The pinched tube problem: the normal curvature κ_x along the axial line $\theta = 0$.

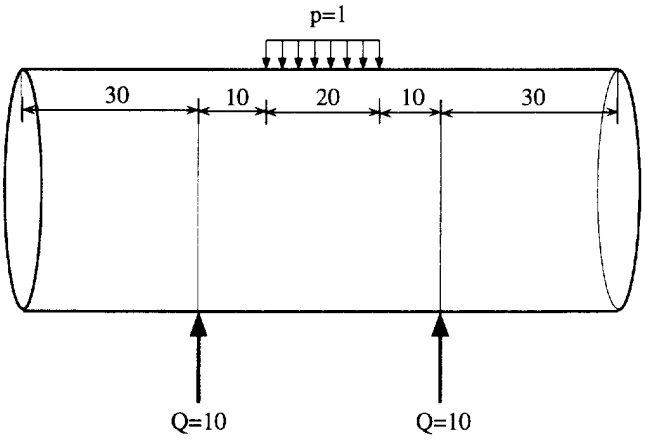

Fig. 9. Set-up of the beam-like loading problem.

or the stress *at the boundary*, and we investigate the rate in which this disturbance decays (if at all) away from this boundary into the interior of the tube. The theoretical treatment of such decay is discussed in Appendix A.

Now we perturb the *shape of the boundary* at the edge $x = 0$. To this end, we replace the boundary condition $\psi = 0$ which was used up till now [see eqn (6)] by the inhomogeneous condition $\psi = 0.01 \cos(2s/R)$ at the edge $x = 0$. This amounts to the *ovalization* of the circular boundary. Note that although in previous sections we considered only homogeneous boundary conditions for simplicity, the extension to inhomogeneous conditions is easy and quite obvious.

We set $L = 1$, $R = 0.1$, $Eh = 6.9 \times 10^7$, $P_x = 1.6 \times 10^4$, and we use 100 identical finite elements. Figure 12 shows the normal displacement $\psi = w$ along the axial line $\theta = 0$ for different values of P_s. We see that for $P_s = 0$, w varies linearly with x. This is exactly the result obtained by linear membrane theory. However, when P_s is increased, the solution is seen to decay away from the edge.

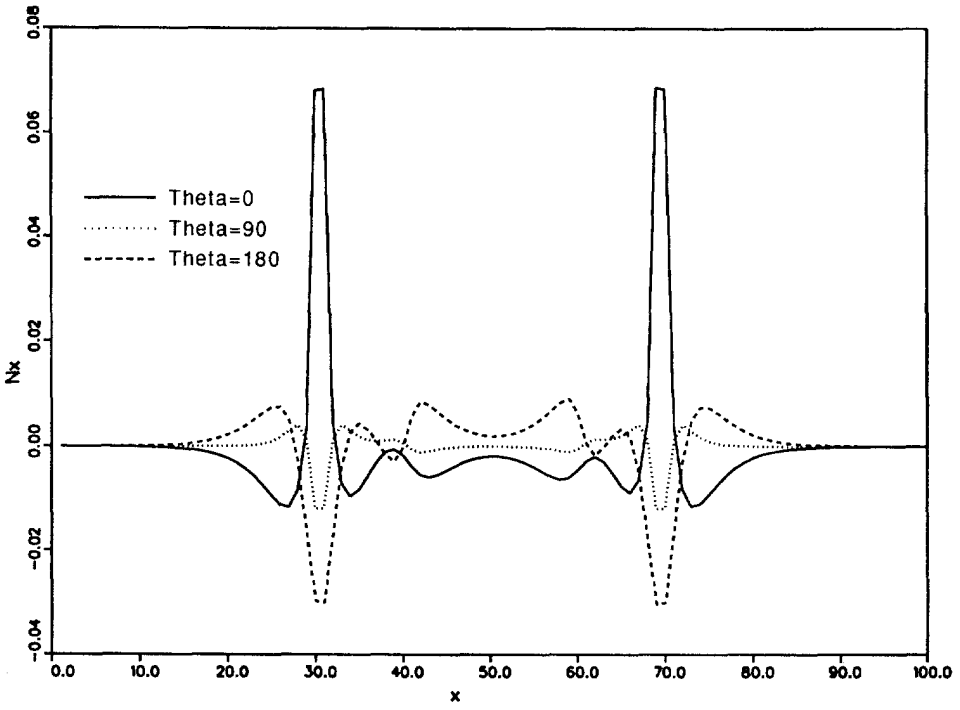

Fig. 10. The beam-like loading problem: the stress N_x along different axial lines.

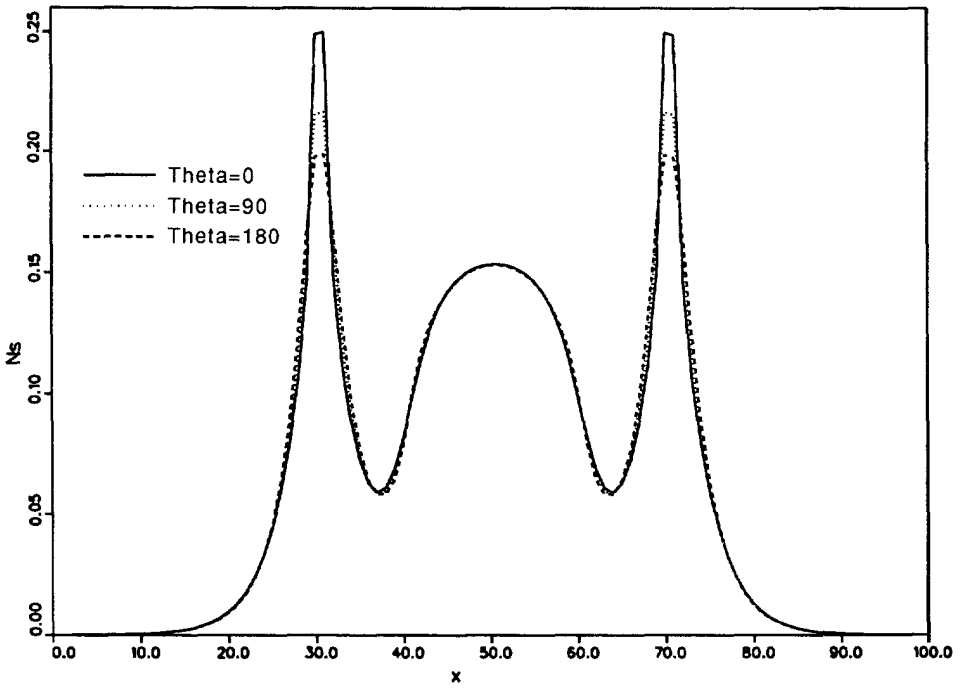

Fig. 11. The beam-like loading problem: the stress N_s along different axial lines.

Example 7: nonuniform boundary tension

In this final example, we perturb the state of stress at the boundary $x = 0$ by applying to the boundary an incremental tensile stress N_x which is in self-equilibrium. This defines a St. Venant type problem. The prescribed tension is of the form $N_x(0, s) = \cos(ks/R)$, where $k \geqslant 2$ is an integer. This boundary condition is imposed in practice by prescribing $\phi(0, s) = -(R/k)^2 \cos(ks/R)$, where we make use of the relation $N_x = \phi_{,ss}$ [see eqn (4)]. We use the same parameters as in example 6.

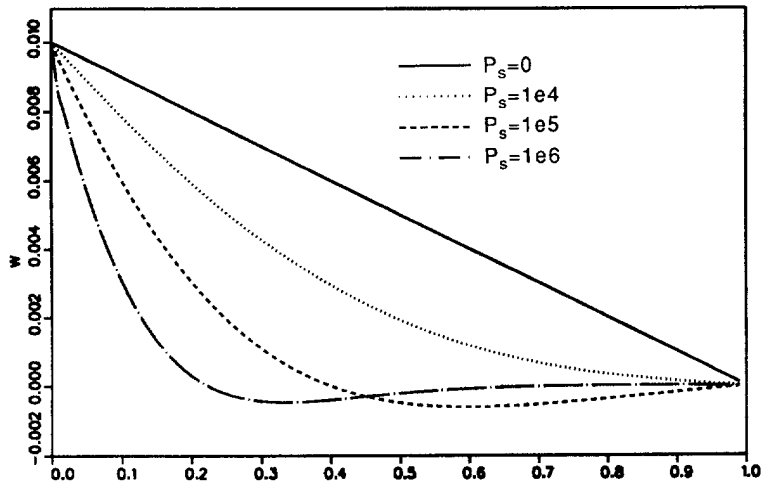

Fig. 12. The boundary ovalization problem: the normal displacement ψ along the axial line $\theta = 0$ for different values of P_s.

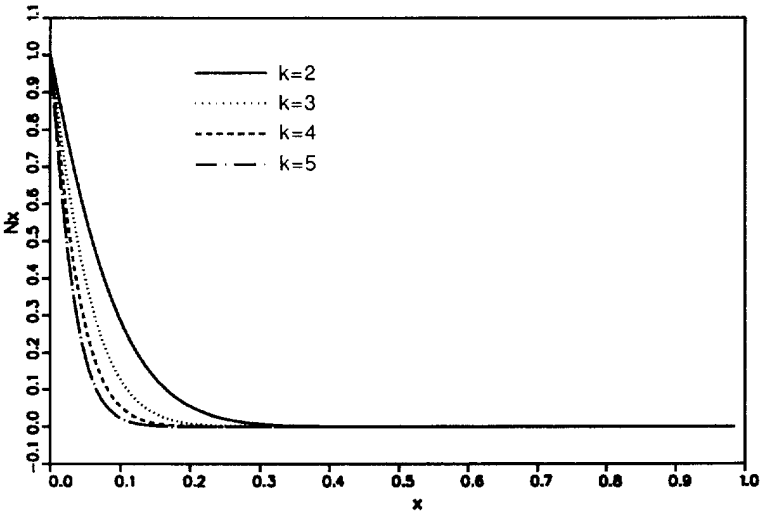

Fig. 13. The boundary tension problem, with $N_x(0, s) = \cos(ks/R)$ prescribed: the stress N_x along the axial line $\theta = 0$ for different values of k.

Figure 13 shows the stress N_x along the axial line $\theta = 0$ for different values of k, with $P_s = 2.8 \times 10^7$. It is clear that the decay of N_x from the boundary of the tube is faster for larger values of k, namely for boundary loads which are more rapidly varying. This result is explained by the self-cancellation effect which is present when the boundary load is highly oscillatory.

Now we fix $k = 2$ and we change the value of P_s. Figure 14 shows N_x along the axial line $\theta = 0$ for different values of P_s. As in the previous example, the result obtained for $P_s = 0$ is the same as that predicted by linear membrane theory, and as P_s is increased, the decay of the solution away from the edge becomes more prominent.

We define the "decay distance" to be the distance from the boundary along the axial line $\theta = 0$, where N_x reaches a value of 5% from the boundary value $N_x = 1$. Figure 15 shows the decay distance as a function of $\log(P_s + 1)$, according to this definition. We see that up to about $P_s = 10^3$ no decay is exhibited at all. Beyond $P_s = 10^3$, the decay distance decreases rapidly with increasing loads P_s. For loads bigger than about $P_s = 10^6$, the decay distance does not decrease any further.

It is seen that the "decay distance" depends on the type of preloading and type of disturbance. For example, in the problem involving an axisymmetric ring load (example 2), the decay distance *increases* with the increase in preloading P_x (Fig. 3), whereas in

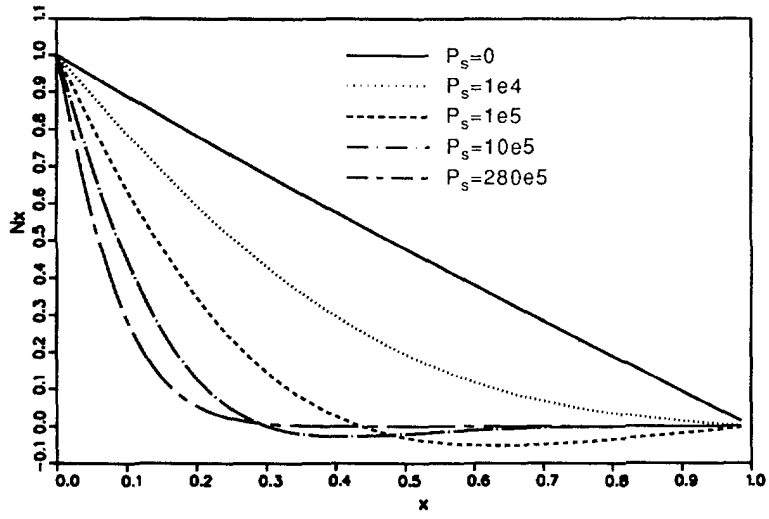

Fig. 14. The boundary tension problem: the stress N_x along the axial line $\theta = 0$ for different values of P_s.

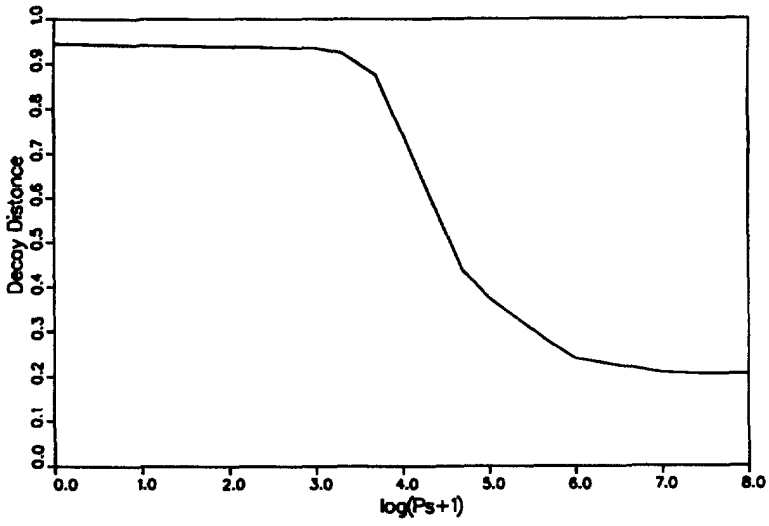

Fig. 15. The boundary tension problem: the "decay distance" as a function of the initial pressure P_s.

problems involving nonuniform edge disturbances (examples 6 and 7), the decay distance *decreases* with the increase in preloading P_s (Figs 12 and 14). A more general analysis of the decay problem is presented in Appendix A. As explained there, both types of behavior can occur, and the proper mixture may depend on the problem at hand.

8. CONCLUDING REMARKS

In this paper we have proposed a numerical scheme for the solution of problems of membrane tubes, which are formulated under the incremental theory developed in the first part of this series (Libai and Givoli, 1994). We have demonstrated the performance of the scheme by applying it to several model problems. The proposed numerical method is based on finite element discretization in the axial (x) direction, and discrete Fourier decomposition in the circumferential (s or θ) direction. The modal decomposition leads to a nonstandard finite element formulation which requires the construction of special finite elements.

One may raise the question whether it may be better to use finite element discretization *throughout* the domain, namely in both x and s, or maybe to apply Fourier decomposition *throughout* the domain. Both options are possible. The former case is discussed in Sections

9 and 10 of Libai and Givoli (1994); the simplest conforming finite element would have 20 degrees of freedom and the whole procedure would entail large computational effort. This is, however, unavoidable if the tube contains slits or holes. On the other hand, the use of Fourier decomposition in both x and s would typically require an extremely large number of harmonics to resolve the local features of $p(x, s)$ in both x and s.

Thus, it seems that for membrane tubes which do not contain holes or slits, the combined use of finite elements and Fourier decomposition leads to a well-balanced scheme, as far as accuracy and computational efficiency are concerned. The advantages of using combined finite element and spectral discretization for the solution of problems in solid mechanics have also been observed in previous works [see e.g. Rand and Givoli (1992), Givoli and Rand (1993), Wunderlich *et al.* (1985), Danielson and Tielking (1993) and Kaiser *et al.* (1993)].

Acknowledgements—The first author acknowledges the support by the M. S. Geltman Memorial Academic Lectureship. Both authors acknowledge the support by the Fund for the Promotion of Research at the Technion.

REFERENCES

Akhras, G., Cheung, M. S. and Li, W. (1993). Static and vibration analysis of anisotropic composite laminates by finite strip method. *Int. J. Solids Structures* **30,** 3129.

Babuska, I. and Szymczak, W. G. (1982). An error analysis for the finite element method applied to convection diffusion problems. *Comput. Meth. Appl. Mech. Engng* **31,** 19.

Bathe, K. J. and Almeida, C. A. (1980). A simple and effective pipe elbow element—linear analysis. *ASME J. Appl. Mech.* **47,** 93.

Calladine, C. R. (1983). *Theory of Shell Structures*. Cambridge University Press, Cambridge.

Cook, R. D., Malkus, D. S. and Plesha, M. E. (1989). *Concepts and Applications of Finite Element Analysis*. John Wiley, New York.

Danielson, K. T. and Tielking, J. T. (1993). Fourier continuum finite elements for large deformation problems. *Comput. Structures* **49,** 133.

Fletcher, C. A. J. (1984). *Computational Galerkin Methods*. Springer, New York.

Givoli, D. (1988). Non-local and semi-local optimal weighting functions for symmetric problems involving a small parameter. *Int. J. Numer. Meth. Engng* **26,** 1281.

Givoli, D. and Rand, O. (1993). Harmonic finite element thermoelastic analysis of space frames and trusses. *J. Therm. Stresses* **16,** 233.

Hughes, T. J. R. (1987). *The Finite Element Method*. Prentice-Hall, Englewood Cliffs, NJ.

Kaiser, T. M. V, Elwi, A. E. and Mioduchowski, A. (1993). A nonlinear axisymmetric finite element for modeling nonaxisymmetric behavior. *Comput. Structures* **49,** 219.

Kikuchi, F. (1987). Mixed and penalty formulations for finite element analysis of an eigenvalue problem in electromagnetism. *Comput. Meth. Appl. Mech. Engng* **64,** 509.

Libai, A. (1972). The nonlinear membrane shell with application to noncircular cylinders. *Int. J. Solids Structures* **8,** 923.

Libai, A. and Givoli, D. (1994). Incremental stresses in loaded orthotropic circular membrane tubes—I. Theory. *Int. J. Solids Structures* **32,** 1907–1925.

Malkus, D. S. and Hughes, T. J. R. (1978). Mixed finite element methods, reduced and selective integration techniques: a unification of concepts. *Comput. Meth. Appl. Mech. Engng* **15,** 63.

Rand, O. and Givoli, D. (1992). Thermal analysis of space structures including three-dimensional effects. *Int. J. Numer. Meth. Heat Fluid Flow* **2,** 115.

Roberts, J. E. and Thomas, J.-M. (1991). Mixed and hybrid methods. In *Handbook of Numerical Analysis* (Edited by P. G. Ciarlet and J. L. Lions), Vol. II, Part 1, p. 523. North-Holland, Amsterdam.

Sewell, M. J. (1987). *Maximum and Minimum Principles*. Cambridge University Press, Cambridge.

Stenberg, R. (1988). A family of mixed finite elements for the elasticity problem. *Numer. Math.* **53,** 513.

Stolarsky, H. and Belytschko, T. (1983). Shear and membrane locking in curved C^0 elements. *Comput. Meth. Appl. Mech. Engng* **41,** 279.

Wunderlich, W., Cramer, H. and Obrecht, H. (1985). Application of ring elements in the nonlinear analysis of shell of revolution under nonaxisymmetric loading. *Comput. Meth. Appl. Mech. Engng.* **51,** 259.

APPENDIX A: DECAY OF DISTURBANCES FROM THE EDGE

Nonuniform input in the form of self-equilibrated forces or geometrical disturbances applied to the edge of a loaded cylindrical membrane should attenuate as the distance from the edge increases. This is in contrast with the linear case ($P_\gamma = P_\zeta = 0$), where attenuation might not occur. Examples include the decay of longitudinal self-equilibrated stresses (St. Venant problem), edge ovalization [which, as shown in Libai (1972), can be used for the analysis of oval membranes by perturbation from the circular form], edge rotations, and so forth. See examples 6 and 7 in Section 7.

To analyse this problem, we consider the homogeneous form of eqns (1) and (2). It is possible to eliminate ψ and to obtain a single sixth-order equation in ϕ, namely

$$R^2\nabla_*^4(P_x\phi_{,xx}+P_s\phi_{,ss})-\phi_{,xxxx}=0. \tag{A1}$$

This is the homogeneous counterpart of eqn (61) of Libai and Givoli (1994). Now we seek a solution of (A1) in the form:

$$\phi = C\exp(-\lambda x/R)\cos(ks/R), \tag{A2}$$

where k is the circumferential wave number of the disturbance and λ is the exponential axial decay coefficient. The resulting characteristic equation for λ is:

$$[\beta_x(k/R)^4+\beta_s(\lambda/R)^4-\rho(k^2\lambda^2/R^4)][P_x(\lambda/R)^2-P_s(k/R)^2]-(\lambda/R)^4=0. \tag{A3}$$

Defining $\bar\beta_x=\beta_x/(Eh)$, $\bar\beta_s=\beta_s/(Eh)$, $\bar\rho=\rho/(Eh)$, $\bar\varepsilon_x=k^2P_x/(Eh)$, $\bar\varepsilon_s=k^2P_s/(Eh)$, $\mu=(\lambda/k)^2$ (where E is a reference elastic modulus), the characteristic equation reduces to

$$(\bar\beta_x+\bar\beta_s\mu^2-\bar\rho\mu)(\bar\varepsilon_x\mu-\bar\varepsilon_s)-\mu^2=0, \tag{A4}$$

which is a *cubic* equation in μ as a function of $\bar\varepsilon_x,\bar\varepsilon_s$, and the orthotropic elastic parameters $(\bar\beta_x,\bar\beta_s,\bar\rho)$. A general solution of the cubic equation is available, from which six values of λ can be obtained. Only these with positive real parts are needed.

Specific cases can easily be studied by analytical or numerical means. In the isotropic case, $\bar\beta_x=\bar\beta_s=\frac{1}{2}\bar\rho=1$, and the characteristic equation becomes:

$$(\mu-1)^2(\bar\varepsilon_x\mu-\bar\varepsilon_s)-\mu^2=0. \tag{A5}$$

Special cases are:

(a) For $\bar\varepsilon_x=\bar\varepsilon_s=\varepsilon$ the equation is $\varepsilon(\mu-1)^3=\mu^2$.
(b) For $\bar\varepsilon_s=0$ the equation is $\bar\varepsilon_x(\mu-1)^2=\mu$, or $\mu=0$.
(c) For $\bar\varepsilon_x=0$ the equation is $\bar\varepsilon_s(\mu-1)^2=-\mu^2$.
(d) For $\bar\varepsilon_s=\eta\bar\varepsilon_x$ the equation is $\bar\varepsilon_s(\mu-1)^2(\mu-\eta)=\mu^2$.

The last case can be used for a parametric study, with η as a parameter. The case $\eta=1/2$ is that of a closed pressurized tube.

The equation is somewhat similar to that obtained for the bending and buckling of cylindrical shells (without the bending term and with different signs), so that fast and slow attenuations are expected to occur (Calladine, 1983).

In the axisymmetric case, the above does not hold, and we must go back to the original equations (23)–(30) of Libai and Givoli (1994). Equation (24) reduces to an identity. From eqns (26)–(28) we find $\kappa_x=\psi_{,xx}$, $\kappa_s=-\psi/R^2$, $\varepsilon_s=-\psi/R$. Equation (23) yields $N_x=N_0+P_s\varepsilon_s-P_x\varepsilon_x$, where N_0 is a constant, to be determined from the end conditions. The constitutive relations (29) and (30) yield $N_x=K_1\varepsilon_x+K_2N_0$, where

$$K_1=\frac{1+c_xP_x+c_{xs}P_s}{c_s+(c_sc_x-c_{xs}^2)P_s},\quad K_2=\frac{c_{xs}}{c_s+(c_sc_x-c_{xs}^2)P_s}. \tag{A6}$$

Finally, the equilibrium equation (25) of Libai and Givoli (1994) reduces to

$$P_x\psi_{,xx}-(P_s+K_1)\psi/R^2=-K_2N_0/R. \tag{A7}$$

Substituting $\psi=C\exp(-\lambda x/R)$ into the homogeneous part of (A7), we obtain the characteristic equation,

$$\lambda^2=(P_s+K_1)/P_x. \tag{A8}$$

If the initial stresses are small compared with Eh, then $K_1\simeq 1/c_s$. In this case, for a given P_s, λ is proportional to $P_x^{-1/2}$.